Far-Field Excitation of a Photonic Flat Band via a Tailored Anapole Mode

Peiwen Ren,[1,*] Junrong Zheng,[1,*] Zhuo Huang,[1,*] Yan Liu,[1] Long Zhang,[1] Hua Zhang,[1] Jingwen Ma,[2] Zhanghai Chen,[1,†] Jian-Feng Li,[1,‡] Jun Yi,[1,§] and Zhilin Yang[1,‖]

[1]*College of Physical Science and Technology, School of Electronic Science and Engineering, State Key Laboratory of Physical Chemistry of Solid Surfaces, College of Chemistry and Chemical Engineering, College of Energy, Fujian Key Laboratory of Ultrafast Laser Technology and Applications, Xiamen University, Xiamen 361005, China*

[2]*Department of Electronic Engineering, The University of Hong Kong, Hong Kong, China*

(Received 25 October 2024; accepted 22 July 2025; published 22 August 2025)

The photonic flat band, defined by minimal dispersion and near-zero group velocity, has facilitated significant advances in optical technologies. The practical applications of flat bands, such as enhanced light-matter interactions, require efficient coupling to far-field radiation. However, achieving controlled coupling between flat bands and their corresponding localized modes with far-field radiation remains challenging and elusive. Here, we achieve the tunable far-field excitation of a flat band in the near-infrared spectral range by coupling it to a photonic anapole mode. Distinct from conventional multipolar resonances in both its physical nature and unique radiation dynamics, the anapole mode offers highly localized field distributions and tunable emission characteristics, enabling the realization of a photonic flat band and precise control over its transition from a nonradiative to a radiative state. We directly observed the flat band within $\pm 25°$ experimentally by angle-resolved far-field transmissivity spectroscopy. Simulation results extending to 90° confirm the persistence of the band's flatness across all incident angles, validating the inherent flatness of the band. Our findings not only provide a viable approach to accessing photonic flat bands but also significantly advance the field of nanoscale photonic manipulation, offering broad potential applications in optical technologies.

DOI: 10.1103/bzpw-7h2x

Introduction—Flat bands in electronic systems are foundational to modern condensed matter physics. Their uniform energy across momentum space and vanishing group velocity induce strong electron localization and enhanced interactions, enabling the study of correlated states and localization phenomena [1–4]. Photonic flat bands represent an analogous phenomenon where light propagation within certain structured materials exhibits minimal dispersion, enabling flexible control over light-matter interactions [5,6]. While electronic and photonic flat bands both stem from wave localization and diffractionless propagation, they differ markedly in how they are realized and in the effects they support [7,8]. The exploration of photonic flat bands, either experimental demonstration or theoretical predictions, has unveiled a host of unique properties and phenomena exclusive to the photonic domain, such as the strongly correlated phase of light, enhanced light-matter interaction [6,9,10], high quality factor resonances [11], slow light [8], and lasing [12,13], promising advances in optical communication, sensing, and information processing.

Inspired by methods used to achieve electronic flat bands, the primary approach to engineering photonic flat bands lies in lattice arrangement manipulation. Geometrically frustrated lattices, such as the Lieb, Kagome, and diamond lattice, have been extensively investigated in coupled waveguide arrays [14–17]. Moiré-induced flat bands in twist bilayer systems have also been demonstrated both theoretically and experimentally [12,18,19]. Recent work reveals that the Landau flat band arises from a strain-induced pseudomagnetic field in photonic crystal slabs [20,21]. While these methods rely on Bloch wave superposition for state localization, photonic systems offer unique advantages, allowing localized states to be engineered at the single-unit-cell level through precise meta-atom design, without requiring extended lattice interactions. Metallic architectures that support surface plasmon resonances offer an effective platform for subwavelength field confinement. However, their practical implementation in flat band systems is constrained by intrinsic Ohmic losses and material-dependent dispersion limitations, leading to reduced Q factors and narrow operational bandwidths [22–24]. Conventional dielectric multipole

*These authors contributed equally to this work.
†Contact author: zhanghai@xmu.edu.cn
‡Contact author: Li@xmu.edu.cn
§Contact author: junyi@xmu.edu.cn
‖Contact author: zlyang@xmu.edu.cn

resonances, however, lack the strong unit-cell field confinement required for flat bands, as their extended fields and intercell coupling prevent effective localization. Embedding meta-atom resonances within photonic band gaps has emerged as a potential solution [25,26], but this approach is limited by strict periodicity requirements, high sensitivity to disorder, and narrow spectral overlap between the resonance and the band gap. Emerging theoretical frameworks have also proposed bound states in the continuum (BIC) as a new platform for Brillouin-zone-spanning photonic flat bands, though experimental validation remains pending [27–29]. Collectively, these developments highlight the potential of constructing a photonic flat band by selecting an intrinsic localized mode in photonic crystals.

Beyond the formation of photonic flat bands, their practical applications, such as enhanced light-matter interactions, require efficient coupling to far-field radiation. Without such coupling, flat bands remain purely theoretical constructs, with their unique dispersion characteristics rendered inaccessible to external excitations. However, this coupling often proves to be weak due to the inherently localized nature of the flat band modes. For flat bands arising from lattice management, it is quite difficult to control the coupling properties once the strategy is determined. One method implemented in waveguide array systems (typically sized at several tens of micrometers) involves using multiple light spots with designed intensity and phase, coupling them into each waveguide to excite the flat band [15,16]. However, this approach becomes impractical for photonic crystals due to the diffraction limit. The coupling properties of flat bands induced by BIC can be tuned quite easily by mode conversion between BIC and quasi-BIC states. However, the Q factor in BIC-driven systems exhibits an inverse quadratic variation with respect to asymmetric parameters, which makes them highly sensitive to perturbations in the geometry or the incident light angle [27,28]. This sensitivity hinders the robust realization of high Q flat bands, particularly over a broad range of incident angles, thus posing a critical obstacle in the development of advanced photonic devices.

Herein, we address this challenge by employing the anapole mode, which is fundamentally distinct from conventional multipolar modes in both physical origin and radiative behavior, to facilitate the far-field excitation of photonic flat bands. This nontrivial mode, supported by high-index dielectric nanostructures, features strong field localization and tunable radiation characteristics, offering a promising route toward the construction of tailored flat bands. We demonstrate that the band associated with the anapole mode exhibits directional dispersionless behavior, attributed to the localized nature of its field distribution. The radiation properties of the anapole mode and the resulting flat band are successfully tuned by controlling the relative strengths of the electric dipole (ED) and toroidal dipole (TD) moments through geometric design. Based

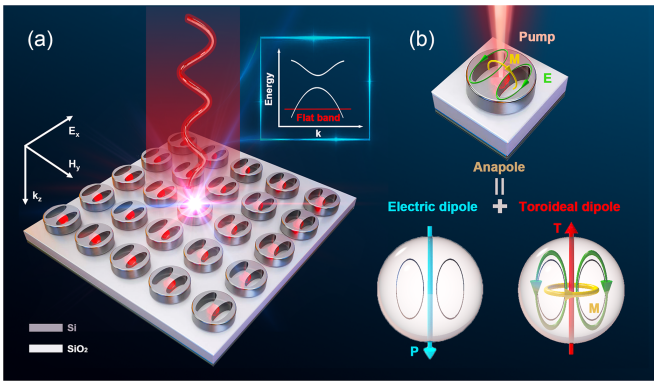

FIG. 1. (a) The schematic illustrates the design of the anapole metasurface, composed of periodic silicon disks featuring two parallel elliptical holes on a quartz substrate. (b) Incident light triggers the formation of an ED oscillation within the bridge spanning two elliptical holes. Concurrently, a pair of counter-rotating vortices emerges (green arrow) within the elliptical holes. The TD moment is associated with the circulating magnetic field (MD, yellow circle) accompanied by an electric poloidal current distribution. The analogous symmetry of the ED and TD modes' radiation patterns leads to destructive interference effects, resulting in the formation of an anapole mode with vanishing scattering and a highly nontrivial field distribution.

on angle-resolved transmissivity spectroscopy, we directly measure the energy band structure of the optimized anapole metasurface in Fig. 1(a), and reveal a clear flat band in the near-infrared spectral region with an ultralow angular dispersion of 0.17 meV/°. This Letter not only demonstrates an innovative method for accessing and utilizing photonic flat bands but also expands the toolkit for nanoscale photonic manipulation, with implications for a wide range of applications in optical technologies and beyond.

Results and discussion—We begin by analyzing a two-dimensional square lattice composed of silicon columns (permittivity values from Ref. [30]). The structure has a period P of 665 nm, with each column possessing a radius R of 275 nm [Fig. 2(a)]. The first few transverse electric (TE) bands are presented in Fig. 2(b). The band structure reveals regions with significant dispersion, as well as areas where the bands are relatively flat. These regions, labeled 1 through 5, show a gradual decrease in dispersion, becoming progressively flatter. The corresponding electric field distributions are shown in Fig. 2(d). It is noteworthy that for dispersive bands, the electric fields are primarily concentrated outside the silicon, while for flat bands, the electric fields are more localized within the silicon. To quantitatively capture this relationship, we define the confinement factor C as the ratio of the electric field energy inside the Si to the total energy within the unit cell, aiming to link it to the formation of flat bands:

$$C = \frac{\iiint_{\text{in}} \varepsilon_r |\boldsymbol{E}|^2 dV}{\iiint_{\text{all}} \varepsilon_r |\boldsymbol{E}|^2 dV} \tag{1}$$

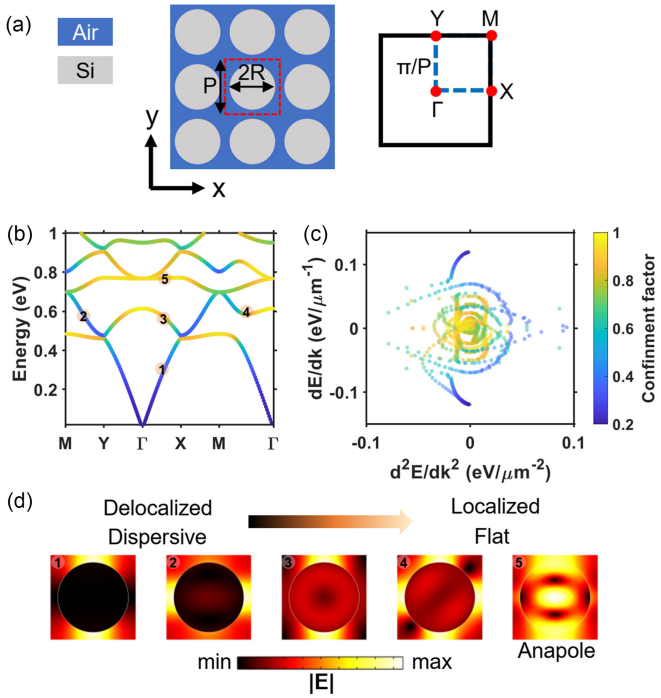

FIG. 2. (a) Geometric unit cell and Brillouin zone of a square lattice composed of Si columns. (b) Band diagrams of the first few TE modes for the lattice, with the confinement factor of each mode at different wave vectors represented by color. (c) Distribution of the confinement factor as a function of the first and second derivatives of energy with respect to wave vector. (d) Typical normalized absolute electric field distributions extracted at the labeled points in (b).

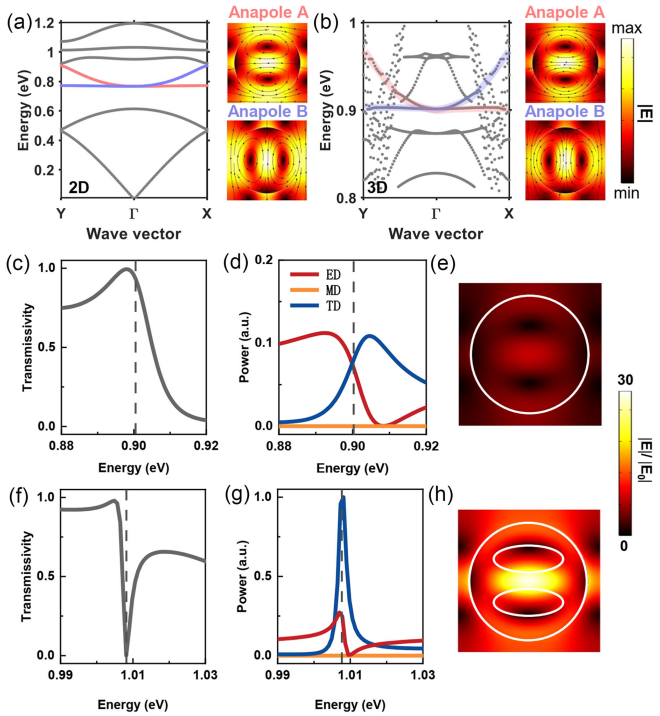

FIG. 3. (a) Enlarged view of the band diagram for the 2D lattice near the flat band, which supports two anapole modes (highlighted in red and blue), with their corresponding field distributions shown on the right. (b) Same as (a), but for a 3D lattice with a thickness of 250 nm placed on a quartz substrate. (c) Simulated transmissivity spectrum of a perfect disk lattice under normal incidence, with the gray dashed line indicating the energy of the flat band mode, as simulated by eigenfrequency analysis. (d) Multipolar decomposition of the flat band mode. (e) Simulated electric field distribution of the lattice under normal incidence at the energy obtained from eigenfrequency analysis. (f)–(h) Same as (c)–(e), but for a disk with two nanopores.

where ε_r is the relative permittivity distribution and E is the complex electric field. This confinement factor C is then plotted as a function of the first and second derivatives of the energy E with respect to the wave vector k to examine its relationship with band dispersion [Fig. 2(c)]. It shows that points with large C tend to cluster near the origin indicating that the band is flat, while those with small C are more dispersed. This approach connects the real-space field distribution of a mode to its band in momentum space, providing valuable insights for designing nanostructures with desired dispersion or predicting the band structure based on the mode's field distribution [Fig. 2(d), right]. Most of the bands shown in Fig. 2(b) do not exhibit flat regions crossing the symmetry points. This can be attributed to the limited dielectric constant of silicon, which restricts conventional resonant modes from supporting highly localized states, thus preventing the formation of flat bands. However, it is noteworthy that around label 5, a flat band appears along the Y-Γ-X direction, and the corresponding electric field distribution exhibits a characteristic anapolelike mode [Fig. 2(d), right]. Anapole mode arises from the coherent superposition of two fundamental electromagnetic entities: the ED and TD [31]. These multipoles exhibit distinct physical origins: the ED stems from charge polarization asymmetry, while the TD is generated by poloidal current loops forming a closed magnetic vortex [Fig. 1(b)] [32,33]. In the far-field region, these modes produce similar radiation patterns and can induce destructive interference, leading to vanishing scattering, along with nontrivial field distributions and strong field confinement [34]. While other approaches, such as defect modes, can also achieve strong field confinement and flat bands in dielectric photonic crystals [25,26], the primary advantage of the anapole mode is its ability to tune radiative properties by adjusting the relative strengths of the ED and TD moments, thereby enabling the realization of flat bands with tunable radiative characteristics.

Figure 3(a) presents an enlarged view of the band structure around the flat band. A detailed analysis of the electric field distribution reveals that the flat band along the Y to X direction results from the superposition of two anapole modes (highlighted in red and blue), with their electric field distributions being mutually perpendicular [Fig. 3(a), right]. The gray arrows in the field distribution

indicate the direction of the electric field, where poloidal current loops that form the TD are observed. Extended simulations demonstrated that the band associated with anapole mode in different types of 2D silicon photonic crystals also supported a flat band in specific directions due to nontrivial field localization (Supplemental Material (SM) [35], Fig. S1). When moving to 3D simulations (disks with finite thickness of 250 nm and placed on quartz substrate), a similar flat band and anapole mode remains except for little energy shift compared with 2D ones [Fig. 3(b)]. A flat band can be easily achieved based on the anapole mode without the need for precise design, making it robust against deviations during the manufacturing process.

Our focus now shifts to the excitation of anapole modes and the associated flat band in the far field, which holds significant promise for practical applications. For the perfect disks on a quartz substrate calculated in Fig. 3(b), the transmissivity spectrum under normal incidence with polarization along the x axis is shown in Fig. 3(c), with the energy of the anapole mode at the Γ point predicted by eigenfrequency analysis marked by a dashed line. Unfortunately, the anapole mode is not visible in the far-field spectrum. We performed multipole expansions in the Cartesian coordinates (SM [35]) for currents inside the unit cell to illustrate the composition of the anapole mode and the coupling mechanism of the anapole mode with external radiation. For perfect disks configuration, the anapole modes originate from the overlap of coexcited ED and TD moments that have almost same scattering magnitude [Fig. 3(d)] and opposite phases [SM [35], Fig. S3(a)]. This leads to the cancellation of their scattering contributions in the far field, isolating the mode from the external radiation field. Since the TD moment is generated by the oscillating current circulating along the toroidal structure [Fig. 3(b)], while the ED moment is primarily associated with the diameter of the disks, we can tune these two moments independently. Here, we selectively manipulate the TD moment to ensure that its far-field radiation does not undergo effective cancellation by the ED moment, thereby facilitating the coupling between the flat band mode and the far-field radiation. Specifically, we regulate the strength of the TD by incorporating air holes at the location of the toroidal current. As illustrated in Fig. S2 (SM [35]), the TD mode's intensity is markedly influenced by nanopores with varying parameters. With the enlargement of the upper nanopore, both the two moments shift towards higher energies, with the TD moment exhibiting a more pronounced enhancement in intensity compared to the ED moment. Figure 3(h) shows the optimized structure composed of a Si disk with two elliptical air holes, where the diameters of the two axes of the ellipse are 325 nm and 125 nm. The decomposed moments reveal that the TD moment is 3.6 times stronger than the ED moment [Fig. 3(g)]. Because of the alteration in spatial symmetry, the phase difference exhibits a slight deviation from π [SM [35], Fig. S3(b)], but this does not affect the fundamental mechanism of anapole excitation. Concurrently, a distinct dip, nearly reaching zero, appears in the simulated far-field transmission spectrum [Fig. 3(f)]. Furthermore, the electric field distribution at resonant energy reveals that the optimized structure achieves substantially enhanced field intensity relative to the perfect disk. [Fig. 3(e) and 3(h)]. These results collectively highlight the strong interaction between the anapole modes in the optimized structure and light. The strategic incorporation of tunable nanopores into the Si photonic crystals introduces a novel dimension of control over both the far-field scattering patterns and the concentration of near-field effects of the anapole mode. The eigenfrequency shift $\Delta\omega$ of a mode due to a small perturbation of the dielectric function $\Delta\varepsilon$ can be expressed as

$$\Delta\omega \approx -\frac{\omega}{2}\frac{\int d^3r \Delta\varepsilon(r)|\boldsymbol{E}(r)|^2}{\int d^3r \varepsilon(r)|\boldsymbol{E}(r)|^2}. \tag{2}$$

Therefore, the introduction of air nanopores causes a shift in the anapole mode to higher energy, as mentioned before. Furthermore, since the electric field distribution of the anapole A remains nearly constant along the path from Γ to X, the energy shift resulting from the perturbation of the dielectric function is also consistent, thus maintaining the flat band. The band simulations of the optimized device confirm the persistence of the flat band characteristics of the anapole mode A along x direction, even as the system undergoes the aforementioned adjustments (SM [35], Fig. S4). This preservation indicates the expected appearance of the flat band in the far-field spectrum, highlighting the robustness of the anapole mode and enhancing the system's overall functionality.

To experimentally validate our proposal, we fabricated the periodic silicon nanoarray by electron beam lithography (SM [35]). Figure. 4(a) presents a scanning electron microscope (SEM) image of the fabricated anapole surface, which aligns well with the design parameters. The silicon photonic crystal structure with height h of 250 nm, period P of 665 nm, and radius R of 275 nm. Each unit cell comprises two identical elliptic nanostructures separated by a 65 nm gap, with long and short axis diameters of 325 nm and 130 nm, respectively. The substrate of the device is SiO_2 and its thickness is about 0.5 mm. The direct measurement of the energy band structure of the anapole metasurface was performed by home-built angle-resolved transmissivity spectroscopy (SM [35], Fig. S5). All measurements were conducted using TM-polarized white light, incident in the x-z plane. As shown in Fig. 4(b), four absorption modes appear, including a pronounced flat band at 1.007 eV with an ultralow average angular dispersion of 0.17 meV/° within 25°. The flat band resonance exhibits a high Q factor of 126 (bandwidth of 7.98 meV) under

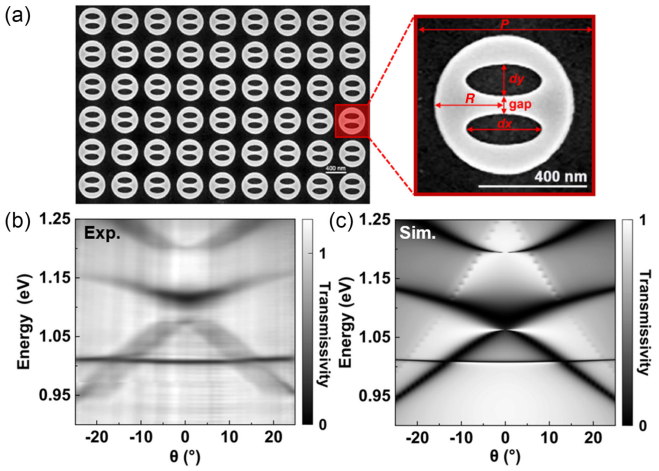

FIG. 4. (a) Scanning electron microscope (SEM) image of the anapole surface. (b) Experimental and (c) simulated angle-resolved transmissivity spectrum with TM-polarized incident light, the wave vector direction of the incident wave is along the x direction. The dispersion of the band position at 1.007 eV is almost negligible, showing the characteristics of a flat band.

normal incidence. Notably, the flat band remains constant in terms of both linewidth and transmission intensity (SM [35], Fig. S6), distinguishing it from the recently theoretically proposed quasi-BIC induced flat bands, where the linewidth significantly varies with angle and totally vanishes at BIC [27–29]. The measured spectra align well with the results obtained from 3D numerical simulations, as shown in Fig. 4(c). Because of the collection objective's numerical aperture being limited to 0.42, photons with emission angles greater than 25° were beyond the measurement capability of our setup. However, simulation results extending to 90° confirm the persistence of the band's flatness across a broad momentum space, validating the inherent flatness of the band (SM [35], Fig. S7). It is noted that the flat band associated with the anapole mode coincides with another dispersive band at approximately 15°, however, due to only a slight overlap between the electric fields of these two modes, no significant spectral splitting occurs (SM [35], Fig. S8), thereby preserving the integrity of the flat band.

Conclusion—In conclusion, we have proposed a flat band with adjustable far-field coupling based on the electromagnetic anapole mode and provided an explanation of the underlying physics behind the flat band formation in the simple lattice. Our Letter bridges the gap between the theoretical potential and practical applications of photonic flat bands, demonstrating both their existence and efficient coupling to far-field radiation. These findings not only enhance our understanding of the conditions necessary for the formation, effective excitation, and visualization of photonic flat bands, but also pave the way for innovative applications in optical technologies, including sensing, computation, and information processing.

Acknowledgments—This work was supported by the National Key Research and Development Program of China (2021YFA1201502), Scientific and Technological Innovation 2030-"Quantum Communication and quantum computer" Major Project (2023ZD0300304), National Natural Science Foundation of China (92161118, 12174324, 21925404, 12304347, and 22272140), Hong Kong Research Grants Council under GRF Grant (17208725), and Fundamental Research Funds for the Central Universities (20720240068).

Author contributions: Conceptualization: Z. L. Y., J. Y., J. F. L., and Z. H. C. Methodology: P. W. R., J. R. Z., Z. L. Y., and J. Y. Investigation: P. W. R., J. R. Z., Z. H., and J. Y. Visualization: P. W. R., J. R. Z., Z. H., Y. L., L. Z., and H. Z. Funding acquisition: Z. L. Y., J. Y., J. F. L., and Z. H. C. Project administration: J. Y. and J. F. L. Supervision: Z. L. Y. and Z. H. C.

[1] Y. Cao, V. Fatemi, A. Demir, S. A. Fang, S. L. Tomarken *et al.*, Nature (London) **556**, 80 (2018).
[2] Y. Cao, V. Fatemi, S. A. Fang, K. Watanabe, T. Taniguchi *et al.*, Nature (London) **556**, 43 (2018).
[3] Y. R. Zhang, R. Polski, C. Lewandowski, A. Thomson, Y. Peng *et al.*, Science **377**, 1538 (2022).
[4] A. Uri, S. c. de la Barrera, M. T. Randeria, D. Rodan-Legrain, T. Devakul *et al.*, Nature (London) **620**, 762 (2023).
[5] L. Q. Tang, D. H. Song, S. Q. Xia, S. Q. Xia, J. N. Ma *et al.*, Nanophotonics **9**, 1161 (2020).
[6] Y. Yang, C. Roques-Carmes, S. E. Kooi, H. N. Tang, J. Beroz *et al.*, Nature (London) **613**, 42 (2023).
[7] P. Wang, Y. L. Zheng, X. F. Chen, C. M. Huang, Y. V. Kartashov *et al.*, Nature (London) **577**, 42 (2020).
[8] T. F. Krauss, Nat. Photonics **2**, 448 (2008).
[9] T. Y. Ning, Y. Y. Ren, Y. Y. Huo, and Y. J. Cai, Front. Phys. **18**, 52305 (2023).
[10] Q. D. Fu, P. Wang, C. M. Huang, Y. V. Kartashov, L. Torner *et al.*, Nat. Photonics **14**, 663 (2020).
[11] R. M. Ma, H. Y. Luan, Z. W. Zhao, W. Z. Mao, S. L. Wang *et al.*, Fundam. Res **3**, 537 (2023).
[12] X. R. Mao, Z. K. Shao, H. Y. Luan, S. L. Wang, and R. M. Ma, Nat. Nanotechnol. **16**, 1099 (2021).
[13] H. Y. Luan, Y. H. Ouyang, Z. W. Zhao, W. Z. Mao, and R. M. Ma, Nature (London) **624**, 282 (2023).
[14] Y. Nakata, T. Okada, T. Nakanishi, and M. Kitano, Phys. Rev. B **85**, 205128 (2012).
[15] S. Mukherjee, A. Spracklen, D. Choudhury, N. Goldman, P. Ohberg, E. Andersson, and R. R. Thomson, Phys. Rev. Lett. **114**, 245504 (2015).
[16] R. A. Vicencio, C. Cantillano, L. Morales-Inostroza, B. Real, C. Mejia-Cortes, S. Weimann, A. Szameit, and M. I. Molina, Phys. Rev. Lett. **114**, 245503 (2015).
[17] L. Morales-Inostroza and R. A. Vicencio, Phys. Rev. A **94**, 043831 (2016).
[18] B. Lou, N. Zhao, M. Minkov, C. Guo, M. Orenstein, and S. Fan, Phys. Rev. Lett. **126**, 136101 (2021).

[19] H. N. Tang, F. Du, S. Carr, C. DeVault, O. Mello *et al.*, Light Sci. Appl. **10**, 157 (2021).
[20] R. arczyk, L. Kuipers, and E. Verhagen, Nat. Photonics **18**, 574 (2024).
[21] M. Barsukova, F. Grise, Z. Y. Zhang, S. Vaidya, J. Guglielmon *et al.*, Nat. Photonics **18**, 580 (2024).
[22] Y. R. Wu, A. E. Hollowell, C. Zhang, and L. J. Guo, Sci. Rep. **3**, 1194 (2013).
[23] J. S. Clausen, E. Højlund-Nielsen, A. B. Christiansen, S. Yazdi, M. Grajower *et al.*, Nano Lett. **14**, 4499 (2014).
[24] X. Wang, T. Sentz, S. Bharadwaj, S. K. Ray, Y. Wang *et al.*, Sci. Adv. **9**, eade4203 (2023).
[25] H. Altug and J. Vučković, Appl. Phys. Lett. **86**, 111102 (2005).
[26] H. Altug and J. Vučković, Appl. Phys. Lett. **84**, 161 (2004).
[27] X. Qi, J. J. Wu, F. Wu, M. Ren, Q. Wei *et al.*, Photonics Res. **11**, 1262 (2023).
[28] Z. Wang, Y. Wang, Z. Cheng, J. Q. Qu, M. J. Cui *et al.*, Appl. Phys. Lett. **123**, 121703 (2023).
[29] Z. Wang, Y. Liang, J. Q. Qu, M. K. Chen, M. J. Cui *et al.*, Photonics Res. **11**, 260 (2023).
[30] M. A. Green, Sol. Energy Mater. Sol. Cells **92**, 1305 (2008).
[31] J. J. Hernandez-Sarria, O. N. Oliveira, and J. R. Mejia-Salazar, Phys. Rev. Lett. **127**, 186803 (2021).
[32] V. Savinov, V. A. Fedotov, and N. I. Zheludev, Phys. Rev. B **89**, 205112 (2014).
[33] N. Papasimakis, V. A. Fedotov, V. Savinov, T. A. Raybould, and N. I. Zheludev, Nat. Mater. **15**, 263 (2016).
[34] T. Zhang, Y. Che, K. Chen, J. Xu, Y. Xu *et al.*, Nat. Commun. **11**, 3027 (2020).
[35] See Supplemental Material at http://link.aps.org/supplemental/10.1103/bzpw-7h2x for the experimental methods, analytical derivations and extended data, which includes Refs. [36,37].
[36] E. E. Radescu and G. Vaman, Phys. Rev. E **65**, 046609 (2002).
[37] A. E. Miroshnichenko, A. B. Evlyukhin, Y. F. Yu, R. M. Bakker, A. Chipouline *et al.*, Nat. Commun. **6**, 8069 (2015).